Ocean Engineering 330 (2025) 121305

Contents lists available at ScienceDirect

Ocean Engineering

journal homepage: www.elsevier.com/locate/oceaneng

Research paper

Aeroelastic investigations of composite blade on floating offshore wind Turbine: Insights into stress responses on multi-hierarchy blade structures

ZhongSheng Deng [a], Qing Xiao [a,*], Liu Yang [b], YuanChuan Liu [c], Enhao Wang [d]

[a] Department of Naval Architecture, Ocean & Marine Engineering, University of Strathclyde, Glasgow, UK
[b] Department of Mechanical & Aerospace Engineering, University of Strathclyde, Glasgow, UK
[c] College of Engineering, Ocean University of China, Qingdao, China
[d] Institute for Ocean Engineering, Shenzhen International Graduate School, Tsinghua University, Shenzhen, China

ARTICLE INFO

Keywords:
Fluid-structure interaction
Composite blades
Floating offshore wind turbine
Surge motion
Stress analysis
Turbulence

ABSTRACT

To improve the blades aeroelastic performance on floating offshore wind turbines, it is essential to analyse the stress conditions and distributions on composite blades. This paper serves as a continuation of the previous work, we examined the impacts of FOWT platform surge periods and amplitudes to the composite blade aeroelastics, with considerations of turbulent effects when solving for the aerodynamic loads. The result shows that a shorter surge period and larger surge amplitude can lead to significant stress amplifications. The stress concentrations are predominantly observed on the blade substructure shear webs, underscoring the need for local stress inspections. A linear relationship between surge amplitude and local max. stress magnitude is identified, which is helpful for a quick preliminary blade design. The findings contribute to the development of more robust and efficient offshore wind energy systems, providing detailed aeroelastic insights for the blade optimizations in the future works.

1. Introduction

In modern wind energy applications, the floating offshore wind turbine (FOWT) applications present significant advantages, such as greater deployment flexibility in deep seas and higher energy production efficiency due to consistent, strong offshore winds (Hollaway, 2013; Edwards et al., 2023). However, the commercialization of FOWT has been hindered due to the severer operation conditions and more sophisticated aeroelastic nonlinearity of the system. These challenges usually lead to unstable power outputs and increase vulnerability of the FOWT system and their component structures, making it an expensive technology for widespread deployments.

The sophisticated physics behind the FOWT blade aeroelastics has yet to be well understood. One key technical challenge is to tackle intensive interactions between the fluid and blade structures induced by the inherent six degrees-of-freedom (DoF) platform motions of the FOWT, thus making it a highly nonlinear aeroelastic problem. Another challenge originates from the further considerations of high-performance composite materials (Z. Zhang et al., 2023), which may introduce additional nonlinearities and exacerbate the blade aeroelastic performance, specifically when the FOWT is operated under extreme environmental conditions.

To enhance and optimize the durability and integrity of the FOWT, comprehensive investigations of the stress performances of operating FOWT blades are essential. Therefore, advanced numerical codes are extensively used to handle the parametric uncertainties and to accurately resolve the highly nonlinear fluid structure interaction (FSI) problem of the FOWT system (Cheng et al., 2019; Otter et al., 2022).

Numerous studies have focused on blade aeroelastic performance of the modern large scale wind turbines (e.g. the NREL 5 MW wind turbine) using the FSI technique for both the bottom-fixed (Yu and Kwon, 2014; Wang et al., 2016; Dose et al., 2018; Miao et al., 2019; Sayed et al., 2019) and the floating (Dai et al., 2017; Liu et al., 2019; Y. Zhang et al., 2023) wind turbine configurations. The predictions of the blade unsteady aerodynamics and the nonlinear loading characteristics of the FOWT, the reduced-order method such as blade element momentum (BEM) or high-fidelity computational fluid dynamics (CFD) approaches (Zhang et al., 2024) are often used, where BEM is a wildly used method due to its excellent computational efficiency (Fritz et al., 2022), while the CFD performs superior accuracy and fidelity by capturing the transient turbulent viscous flows and the fluid interactions in three-dimensional space.

* Corresponding author.
E-mail address: qing.xiao@strath.ac.uk (Q. Xiao).

https://doi.org/10.1016/j.oceaneng.2025.121305
Received 5 January 2025; Received in revised form 27 March 2025; Accepted 17 April 2025
Available online 21 April 2025

For example, Liu et al. (2019) investigated the NREL 5 MW FOWT blade aerodynamics under a prescribed platform surge motion, revealing a time-lag between aerodynamic loads and surge motion, which significantly affects the apparent wind speed, angle-of-attack (AOA), and thus, lead to large amplitudes variations of instantaneous thrust and power. Yang et al. (2023) conducted a CFD study using the actuator curve embedding (ACE) method to evaluate the impact of platform surge motion on rotor aerodynamic thrust and power for a NREL 5 MW FOWT. They found that while mean rotor thrust and power were slightly influenced under surge motion, the instantaneous thrust and power experienced significant overshoots when the platform surged against the incoming flow.

These findings highlight that platform surge motion's periods and amplitudes can significantly affect rotor aerodynamic performance, making it a parameter-sensitive problem. As pointed out by several aerodynamic studies in case of rigid blades (Fang et al., 2021; Sun et al., 2023), the platform surge motion is one the dominating contributors to the rotor aerodynamic uncertainties of an FOWT, which affects the blade structural dynamic response during operations.

Under such platform-induced loads and intensified fluid structure interactions, the assessments of the blade's structural response and stress distributions in composite materials requires in-depth finite element analysis (FEA), where the anisotropic composite properties and non-consecutive composite layups should be taken into consideration. However, due to the high computational costs, few FSI studies were found (Wang et al., 2016; Dai et al., 2017; Miao et al., 2019; Y. Zhang et al., 2023) incorporated FEA codes in investigating the blade stress performance.

A one-way FSI investigation conducted by Y. Zhang et al. (2023), examined a 117 m long composite blade on the IEA 15 MW reference floating wind turbine, revealing a more significant amplification in max. Von Mises (VM) stress under platform-induced loads compared to bottom-fixed conditions. Wang et al. (2016) and Miao et al. (2019) explored related topics with one-way and two-way strong coupling FSI for bottom-fixed turbines.

However, to the author's knowledge, studies using two-way strong coupling FSI for FOWT composite blade aeroelastics have not been broadly reported. For one-way FSI, it often performs less accurately in capturing blade aerodynamics in nonlinear aeroelastic problems (Lamei and Hayatdavoodi, 2020), especially when large blade displacements occur, leading to synchronization issues between the coupling interfaces, and finally lead to inaccurate predictions of the blade aeroelastic responses.

Therefore, this continuation study comprehensively investigated the composite blade aeroelastic performance on a NREL 5 MW FOWT structural stress distributions under prescribed platform surge motion, using the previously proposed effective general-purpose two-way FSI analysis framework (Deng et al., 2024). The multi-hierarchy composite structures are effectively considered. The relationship between the peak stress and varying platform motions of FOWT are quantified. Detailed stress distributions on the composite structures are identified, showing the susceptible locations on the composite blade and offering quantitative insights into the relationship between the surge-induced loadings and the blade aeroelastic and stress performance.

The numerical specifications and backgrounds are introduced in Section 3; Section 4 gives a detailed introduction for the NREL 5 MW blade geometry and the discretised domains in the fluid and structure fields; The selections of FOWT prescribed surge motion load cases are explained in Section 5; Section 6 validates the presented numerical methods and the CFD mesh accuracy; The results of aerodynamic and structural performance are analysed in Section 7.

2. FSI framework

To briefly introduce the effective general-purpose FSI framework proposed in our previous work (Deng et al., 2024), as demonstrated in Fig. 1, the FSI framework consists of three decomposed procedures in a sequential order.

1) Composite blade FEA modelling in Abaqus. To build the fully-resolved composite structural finite element (FE) model, and extract the composite structure mass properties (CSMP) and effective stiffness matrices (ESMs), where the ESMs can be derived via the composite cross-section analysis codes such as VABS (Cesnik and Hodges, 1997; Yu et al., 2002; Chen et al., 2010) and PreComp (Bir, 2001).
2) Two-way strong coupling FSI calculations. Using OpenFOAM and MBDyn as the fluid and structural participants, respectively, for resolving the aerodynamic forces and structural kinematics. Note that the stiffness properties of the actual composite structure in 3D is equivalised into 1D form ESMs, which can be fed to MBDyn model for a reliable prediction of the structural dynamics.
3) Static analysis in FEA. To resolve for the stress distributions on the composite FE model in Abaqus CAE. Once the FSI calculation is finalised, the structural deflections can be extracted and applied to the composite FE model established early in Procedure 1 for resolving the stress distributions in the composite blade structure.

3. Numerical methods

3.1. Fluid solver

3.1.1. Governing equations and discretization

To handle the transient flows under a case where the dynamic sliding mesh is involved in the computational domain, the transient solver pimpleDyMFoam in the finite-volume-based CFD code OpenFOAM (Jasak et al., 2007) is used to solve the Unsteady Reynolds-Averaged Navier-Stokes equations (URANS). The governing equations accounting for the incompressible viscous effects being solved in OpenFOAM are:

$$\nabla \cdot \boldsymbol{U} = 0 \tag{1}$$

$$\frac{\partial \boldsymbol{U}}{\partial t} + \nabla \cdot (\boldsymbol{U} - \boldsymbol{U}_g)\boldsymbol{U} = -\frac{\nabla p}{\rho} + \nabla \cdot \left[\nu_{eff}\left(\nabla \boldsymbol{U} + (\nabla \boldsymbol{U})^T\right)\right] \tag{2}$$

where $\boldsymbol{U}$ and $\boldsymbol{U}_g$ denote the velocity vector in the fluid field control volumes and the sliding mesh nodes, respectively; ν_{eff} stands for the effective kinematic viscosity of the fluid, accounting for the fluid kinematic viscosity ν and eddy viscosity ν_t. The PISO-SIMPLE (PIMPLE) algorithm is adopted as the pressure-velocity coupling scheme to restrict the validity of the momentum predictions $\boldsymbol{U}$ as governed by the continuity equation as presented in Eq. (1).

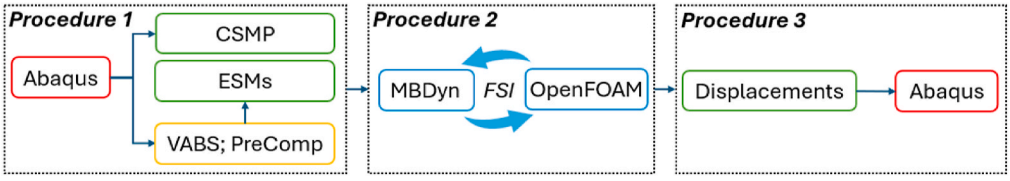

Fig. 1. Diagram of the proposed FSI framework of stress analysis (Deng et al., 2024).

An implicit second-order backward differencing scheme is employed for the temporal term. For gradient calculations, the cell-limited Gauss linear second-order scheme is applied. The default Gauss upwind scheme is used for the convective terms which provides sufficient stability for solving turbulent kinetic energy and specific dissipation rate. To enclose momentum equation in the URANS, the $k-\omega$ Shear Stress Transport (SST) two-equation eddy-viscosity turbulence model (Menter et al., 2003) is adopted to approximate the shear stress aroused from the turbulent flow in the present high Reynolds Number problem.

3.1.2. Mesh motions

An in-house code library is used to simultaneously consider global rotation, platform surge, and blade deflections, by coupling the functionality of the Arbitrary Mesh Interface (AMI) sliding mesh technique (Chandar and Gopalan, 2016) and the inverse distance Laplace equation model (Jasak and Tukovic, 2006) for the deformed mesh nodes updates, expressed as:

$$\nabla\cdot(\gamma\nabla\boldsymbol{u}) = 0, \gamma = \frac{1}{r^2} \tag{3}$$

where r is the nodal offset distance, γ computes the quadratic inverse of the nodal offset distance, which is a diffusivity metric controlling the rapidness of the dynamic motion transitions from the wall boundaries to its adjacent cells. A Laplacian equation is then solved by substituting the nodal displacement vector $\boldsymbol{u}$ to calculate the new location of the mesh nodes of the adjacent cells around the wall boundaries.

3.2. Structure solvers

3.2.1. Motion equations and viscoelastic formulations in MBDyn

The beam-element multibody dynamics (MBD) method has been extensively adopted in many studies with proven capability in predicting the structural dynamics accurately (Simeon, 2006; Bauchau and Nemani, 2021). In FSI process, the MBDyn code solves for the dynamic responses of the structure defined by the three-node beam element model (Ghiringhelli et al., 2000). The linear viscoelasticity properties are assigned to the beam cross-section by considering 6× 6 symmetrical stiffness matrices with proportional damping, accounting for the equivalent stiffness properties of a 3D composite blade structure. The resultant internal stress $\boldsymbol{\sigma}(t)$ with given strains $\boldsymbol{\varepsilon}(t)$ is formulated in a simplified variant of Rayleigh damping form:

$$\boldsymbol{\sigma}(t) = \boldsymbol{D}\boldsymbol{\varepsilon}(t) + \boldsymbol{\eta}\dot{\boldsymbol{\varepsilon}}(t) \tag{4}$$

$$\boldsymbol{\eta} = k\boldsymbol{D} \tag{5}$$

$\boldsymbol{D}$ is the generic form of cross-sectional stiffness matrix and $\boldsymbol{\eta}$ is the viscosity matrix. k is the proportional factor of 0.01 which is applied to all beam elements for preventing numerical instability, as suggested by Resor (2013). An example $\boldsymbol{D}$ in diagonal form is written as follows, representing respectively the shear stiffnesses on the local in and out-of-plane directions; axial stiffness; edgewise and flapwise bending stiffnesses and torsional stiffness:

$$\boldsymbol{D}_{ii} = \{GA_y, GA_z, EA, EJ_y, EJ_z, GJ\} \tag{6}$$

Under the holonomic kinematic constrains, a Newton-Euler motion equation in an implicit differential-algebraic equation (DAE) form is used to provide a generically expression as (Masarati et al., 2014):

$$\boldsymbol{M}(\boldsymbol{x})\dot{\boldsymbol{x}} = \boldsymbol{p} \tag{7}$$

$$\dot{\boldsymbol{p}} + \phi_x^T\lambda = \boldsymbol{f}(\boldsymbol{x}, \dot{\boldsymbol{x}}, t) \tag{8}$$

$$\phi(\boldsymbol{x}, t) = 0 \tag{9}$$

where $\boldsymbol{M}$ is the mass matrix dependant on the nodal system $\boldsymbol{x}$ in 3D Cartesian coordinates; $\boldsymbol{p}$ is the nodal momentum; $\boldsymbol{f}$ accounts for the force and moment vectors; the term ϕ_x^T denotes the Jacobian transpose of the constraint equations with respect to the corresponding nodes in $\boldsymbol{x}$, solving for the forces and moments; λ is the Lagrange multiplier indicating the determinations of the nodal kinematics under given constraints. The boundary conditions are formulated in Eq. (9), defining the regulated nodal kinematics by the holonomic constraints.

3.2.2. Thin shell model in FEA

The fully-resolved composite blade is build using Abaqus FEA, as previously introduced in the FSI framework. The general-purpose finite-strain four-node shell element with reduced integration (S4R) (SIMULIA, 2014) is adopted for modelling the composite blade in Abaqus. The element size of the FEA model is 0.1 m, which has been validated to be a satisfyingly suitable element size for accurate structural predictions as it was indicated from previous study (Deng et al., 2024).

3.3. FSI coupling and data interpolation

As shown in Fig. 2, the solver communications are initialised in the beginning of the analysis via the TCP/IP socket. The convergences of the force and displacement are controlled by OpenFOAM and MBDyn code in a partitioned scheme. The interpolation of displacement occurs at each iteration for the mesh updates in OpenFOAM, while the force is interpolated at the end of each timestep to MBDyn for updating the structural kinematics. The iterative process will continue until the stopping conditions are met.

A schematic diagram of the data interpolation is shown in Fig. 3. A bilinear distance-weighted interpolation scheme is adopted, formulated as:

$$\boldsymbol{K} = \alpha(\boldsymbol{k}_{i-1} + \boldsymbol{R}_{i-1}\boldsymbol{d}_{i-1}) + (1-\alpha)(\boldsymbol{k}_i + \boldsymbol{R}_i\boldsymbol{d}_i) \tag{10}$$

$$\alpha = \frac{\boldsymbol{n}\cdot\boldsymbol{d}}{|\boldsymbol{n}|^2} \tag{11}$$

$\boldsymbol{K}$ represents the new coordinates of node A0, while $\boldsymbol{k}$ signifies the displacement of the structural node. $\boldsymbol{R}$ denotes the quaternion matrices, which handle the node transformations resulting from the rotation of structure nodes. $\boldsymbol{d}$ represents the vector distance from the aerodynamic centre of the patch to the surface node A0. $\boldsymbol{n}$ indicates the vector from its adjacent structure Node i-1 to Node i. Finally, α represents the weighting factor for the dynamics interpolations onto the blade surface node, derived from the distance projection from $\boldsymbol{d}$ to $\boldsymbol{n}$.

The patch centre for each patch section is defined by the aerodynamic centre of the cross-section airfoil at the middle of each patch. For a better synchronization of force and displacement mapping during the FSI process, the structural node and corresponding aerodynamic centre of each patch are overlapped in space, which marks as the coupling points.

4. Model specifications

The NREL 5 MW reference FOWT is used for the aeroelastic investigation in this study. In this section, descriptions for geometry preparations, mesh specifications and composite blade model validations are given in detail.

4.1. Geometrical definitions

The blade geometrical definitions of the NREL 5 MW reference wind turbine and the ones adopted by the present study are listed below in Table 1. According to the blade aeroelastic case studies conducted by Dose et al. (2018), in numerical investigations, the presence of turbine configurations, such as shaft-tilt and pre-cone angles, can influence the aerodynamic force normal to the rotor plane, resulting in the forces with different phases and magnitudes. However, such impact to the blade

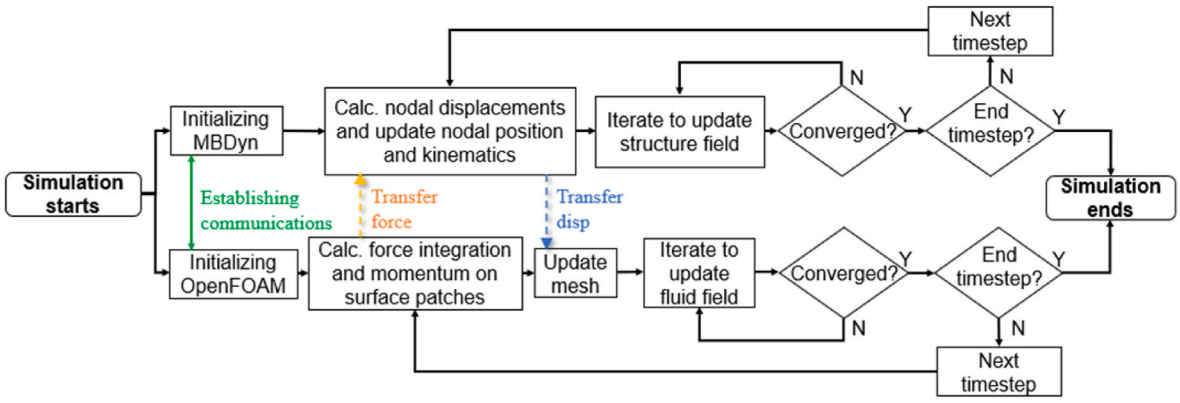

Fig. 2. Schematic diagram of the FSI framework coupling procedure.

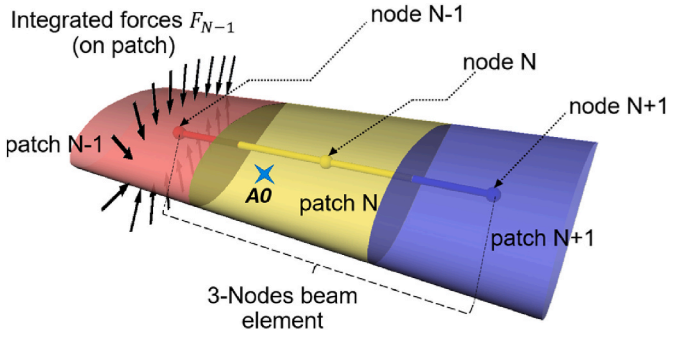

Fig. 3. Schematic diagram of data interpolations between blade patches and structure nodes (Deng et al., 2024).

Table 1
Geometrical definition between the reference and present adopted values.

Definitions	Reference values	Present values
Rotor orientation, # of blades	Upwind, 3 blades	Upwind, 3 blades
Rotor, Hub diameter (m)	126, 3	126, 3
Blade length (m)	61.5	61.5
Overhang (m)	5	0
Shaft-tilt (degree)	5	0
Pre-cone angle (degree)	2.5	0

structural response is found to be insignificant in these cases. Knowing this, we simplified the geometrical setup by excluding the effects of the overhang, shaft-tilt and pre-cone angles in the present study by setting the value to zero. This accelerates the preparations of the blade geometry and dynamic mesh configuration in the FSI simulations.

4.2. CFD domain and mesh

In the present study, the computational domain is divided into 2 regions, the rotor and stator cell zones. The blades (rotor) are placed at the origin of the global coordinate system. To mitigate boundary effects and potential flowing disturbance, as shown in Fig. 4, a large computational domain is given, measures as 15D × 10D × 10D in X, Y and Z directions in space, respectively. The radius of the internal rotor cell region Rc = 150 m, and it spans L = 200 m in X direction. This offers a sufficient space for the flexible blades to deform during the FSI process, preventing the blade wall boundaries from colliding with the interfaces of the sliding mesh. This may also avoid mesh quality deterioration due to the undesired collapse of the cells, especially in the blade tip regions.

To properly reflect the aerodynamic shape of the NREL 5 MW wind turbine blade in the CFD mesh, as shown in Fig. 5, a tight spacing at the

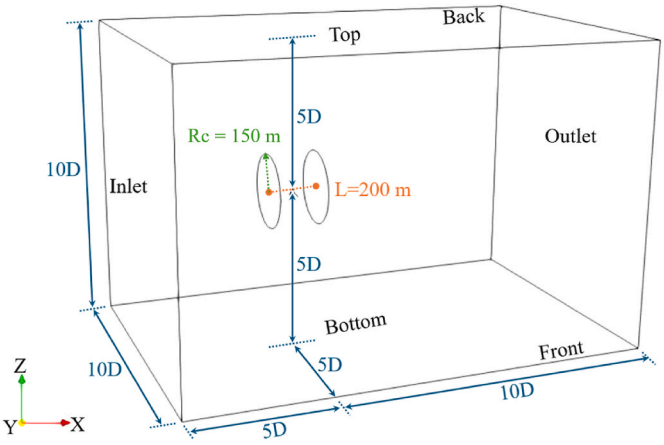

Fig. 4. Computational domain dimensions.

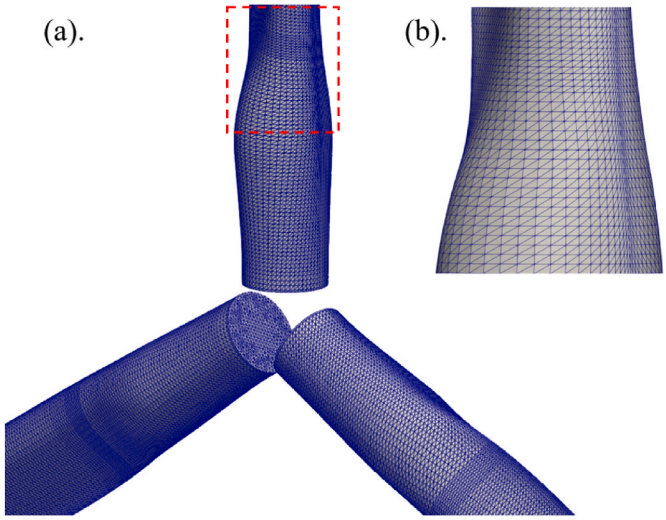

Fig. 5. Leading edge spacing for curvature capturing. (a). the isometric view at the rotor centre; (b). the zoom-in view of the blade.

leading edge is applied to capture the curvature of the blade. Given that the local near wall velocity around the blades is varying during the dynamic simulation, especially when the blade flexible deformation is coupling the platform surge motions, a good quality inflation layer mesh is needed. A well-tuned boundary layer mesh with prism layer cells is applied to the blade surface (Fig. 6), where the first cell height on the

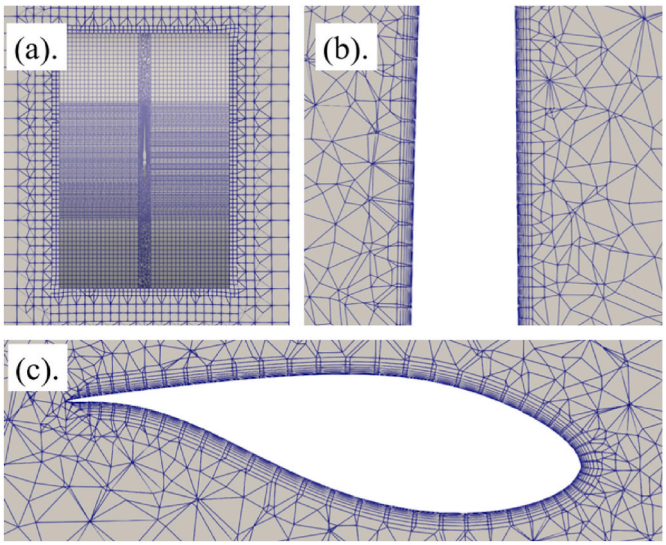

Fig. 6. (a). Overall mesh from the side view; (b). the boundary layer mesh on blade spanwise direction; (c). the boundary layer mesh around the blade cross section.

blade surfaces is 0.002 m with an expansion ratio of 1.25. The blade wall y+ is checked and constrained within the range of 30–300 to assure a reliable performance of the wall functions, so that the near wall flows and resultant forces can be properly predicted across all possible velocity profiles in our present load cases.

It is worth noting that the wake is not the focus of the present study, therefore, the wake region mesh is not being refined, thus it significantly saves the cells in the computational domain, resulting a total number of cells of 3.72 million. A more detailed comparison that validates the current mesh accuracy is given in Section 6, where the aerodynamic thrust, power and the flexible blade tip displacement are compared with several numerical studies from the open literatures.

4.3. Composite blade and material specifications

Fig. 7 displays the blade finite element model that is used for resolving the Von Mises (VM) stresses. A truncation has been implemented on the blade tip to avoid potential mesh deterioration during the numerical process. This leads to a slightly shorter blade model is being used in our studies. The modified blade length (including the distance between hub centre and blade root, L_r) is $R_0 = 61.34$ m.

The composite blade modelling process follows the detailed material definitions, layup distributions and composite stacking specifications as provided by Resor (2013) for the NREL 5 MW reference wind turbine blade. To ensure the composite blade can provide reliable structural responses, important blade properties such as the blade mass and mode of frequencies has been validated in our previous study (Deng et al., 2024), as listed in Tables 2 and 3.

Table 2
Blade mass properties comparisons (Deng et al., 2024).

Descriptions	Desired	Resor (2013)	Present Model	Diff to desired values
Mass (kg)	17740	17700	17435.87	−1.71 %
Mass centre* (m)	20.475	19.102	19.79	−3.35 %
1st mass moment of inertia** (kg m)	3.63E+05	3.38E+05	3.45E+05	−5.00 %
2nd mass moment of inertia** (kg m^2)	1.18E+07	1.10E+07	1.11E+07	−5.74 %

Note: *. Locate on blade spanwise direction; **. With respect to the rotation centre of the blade.

Table 3
Modal frequency comparisons (Deng et al., 2024).

Mode #	Frequency (Hz)		Diff	Description
	Ansys (Resor, 2013)	Present		
1	0.87	0.86	−0.77 %	1st flapwise bending
2	1.06	1.10	+3.79 %	1st edgewise bending
3	2.68	2.72	+1.38 %	2nd flapwise bending
4	3.91	3.94	+0.75 %	2nd edgewise bending
5	5.57	5.51	−1.00 %	3rd flapwise bending
6	6.45	6.36	−1.40 %	1st torsion

5. Determination of surge load cases

To replicate the impacts of the wave-induced platform motions to the blade aeroelastic performance on an FOWT, the surge motion is considered in this study as it is one of the dominating motions that can bring significant instability to the blade aeroelastic performances. A prescribed sinusoidal surge motion equation is applied to the rotor centre, imposing a periodic oscillation to the rotor centre, formulated as:

$$S(t) = ramp(t) \cdot A_S \cdot \sin\left(\frac{2\pi}{T_S} \cdot t\right) \tag{12}$$

$$ramp(t) = k \cdot \begin{cases} 0 & t = 0 \\ t - t_0, & (t_0 \le t \le t_{end}) \\ t_{end} - t_0, & (t_{end} \le t) \end{cases} \tag{13}$$

where, the A_S and T_S are the amplitude and the period of the prescribed surge motion, respectively. The $ramp(t)$ function guarantees a gradual exerting process of platform motion to the rotor, preventing numerical instability at the initial stage of the FSI simulation. k controls the slope of the $ramp(t)$ function. t_0 and t_{end} are the functional time of the $ramp(t)$ function.

Before deciding the prescribed surge motions, we briefly summarised several existing parametrical studies who also adopted the sinusoidal definition for prescribing the platform surge motion load cases, as listed in Table 4. All of the listed studies were focusing on the aerodynamics of the rigid blade on the NREL 5 MW reference wind turbine, where the blade flexibility was not considered.

The selection of surge amplitudes and periods varies widely due to

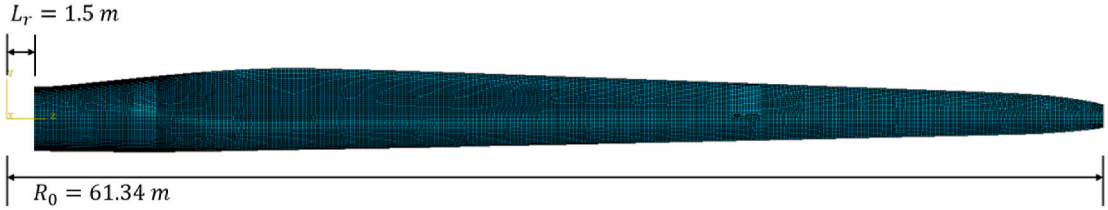

Fig. 7. Blade finite element model established in Abaqus CAE.

Table 4
Selection of prescribed platform motions specifications conducted for the rigid full-scale NREL 5 MW FOWT aerodynamics studies.

Studies	Numerical methods	Prescribed motions A_S (m), T_S (s)	Wind speed, U_0 (m/s)	Rotation speed, Ω_0 (rpm)
Sun et al. (2023)	CFD	A_S = 0.916, 1.348, 2.56 T_S = 12.67, 13.33, 15.38	11.4	12.1
Yang et al. (2023)	CFD	A_S = 2, 4, 6 T_S = 10.00, 15.00, 20.00	11.4; 18	12.1
Lienard et al. (2020)	CFD	A_S = 8, 16 T_S = 9.92	11.4	12.1
Wen et al. (2017)	CFD	A_S = 1.5 T_S = 5.00, 10.00, 33.33	11.4	13.8
Tran and Kim (2016)	CFD	A_S = 8 T_S = 8.16, 12.56, 25.64, 50.00	11.2	12.1
Micallef and Sant (2015)	BEM	A_S = 2.125, 2.15, 2.2 T_S = 9.00	11.4	7.08; 12.39; 19.47
De Vaal et al. (2014)	BEM	A_S = 4, 8, 16 T_S = 8.16, 12.56, 25.51, 49.50	11.2	12.1

different ocean conditions, so that a wide range of parameters can be adopted. In general, severe load cases reveal nonlinear aeroelastic performance with notable dynamic behaviours but may bring difficulties in maintaining the numerical stability. Therefore, the selections of surge motion parameters are based on the literature values in Table 4, to ensure realistic load cases are investigated for obvious observations of blade aeroelastic performances, and meanwhile maintaining the robustness of the numerical process. The specifications of the surge motions in the present study are listed below in Table 5. Two groups accounting for the load cases with different surge periods and amplitudes are divided as G1 and G2, respectively, for the convenience of the result presentations in Section 7.

6. Numerical validation

In this section, the numerical accuracy of the NREL 5 MW FOWT blade aeroelastic performances is validated, considering the platform surge motion. Validations for the bottom-fixed NREL 5 MW wind turbine can be retrieved from our previous study (Deng et al., 2024) for a complete record. A code-to-code comparison against the results from Liu et al. (2019) is conducted in this section, using an identical load case of LC3 (As = 2 m, Ts = 12 s) with identical initial flowing conditions applied. Normalisation of the period is implemented for a clearer comparison of the thrust and power in time domain.

The time histories of thrust and power within one complete period of surge motion are displayed in Fig. 8(a) and (b). It can be seen that the present thrust and power both agreed well with the results from the FSI and the FAST simulations. The variations of the max. thrust between the present and two counterpart studies are 3.75 % and 6.96 %, respectively. Additionally, the structural dynamics is also validated by tracking the flapwise deflection at the blade tip within one surge motion period, as shown in Fig. 8 (c), where it can be seen that the resultant blade tip deflection during one surge period is well agreed with the literature result, with a small difference between the max. deflection of approximately 4.41 %. The results shows that when exposed under the prescribed surge motion, the aerodynamic and structural responses of the blade can be well captured with satisfying accuracies.

Such reasonably small discrepancies in max. quantities comparing to the FSI counterpart's results can be explained. On the one hand, the mesh configurations such as total cell number, wall y-plus distributions and transitions in cell size are different. On the other hand, the counterpart FSI implemented the bounded corrections in spatial discretization, which may impose artificial limits to the field quantities during numerical process, thus has been removed from the current study.

7. Results and discussions

In this section, we presented and discussed the results of the blade aerodynamic and structural behaviours under the designated surge motion load cases, in Section 7.1 and 7.2, respectively.

7.1. Thrust and power

Fig. 9 depicts the aerodynamic thrust and power of all load cases versus the normalised platform surge periods. In G1 plots, the varying magnitudes of thrust and power are inversely related to the surge period, indicating that a shorter surge period can result in greater flapwise load on the blade.

For comparisons in G2, the thrust and power variation increase as the surge amplitude becomes larger. Particularly, from the LC9 results, an instantaneous rotor aerodynamic fluctuation can be clearly observed, with an obvious forward shift from the 2/4T.

This reflects that the evolution of the aerodynamic thrust and power of an FOWT is asymmetrical, due to the coupling effects of the platform surge motion, the constant incoming flow and the elastic blade structure.

To better understand such aerodynamic evolution, an example of LC1 (As = 2m, T = 6s) is given in Fig. 10. In the frontal half-period from 0T to roughly 2/4T, the rotor firstly travels to the max. surge distance on the downstream (point a to b), then reverses its direction towards the upstream. The max. relative velocity U_{re} of V1, defined free stream velocity U_0 minus platform surge velocity U_{surge}, is then reached when the rotor arrives at the surge origin (point c), causing the highest relative velocity on the rotor. The U_{re} reaches to its minimum V2 when the rotor returns to the surge origin at point e. The delays of Δ1 and Δ2 are both seen for the occurrence of the max. and min. thrusts, with respect to V1 and V2.

This reflects that the thrust evolution on the blade always lags behind the relative velocity, which leads to an unbalanced process in the thrust. Specifically, the duration for the thrust increase to its maximal is shorter to that to its minimal. Such asymmetrical behaviour can be especially significant for a more severe load case, where the thrust increases rapidly and decreases relatively slower in a surge period. This may bring in additional instabilities in both structural and aerodynamics to the

Table 5
Load case specifications of different surge motions.

Load Case type	Bottom fixed	Platform surge motion									
Load Case ID	LC0	LC1	LC2	LC3	LC4	LC5	LC2	LC6	LC7	LC8	LC9
Groups	/			G1					G2		
A_S (m)	/	2	2	2	2	2	2	3	4	5	6
T_S (s)	/	6	9	12	15	18	9	9	9	9	9
U_0 (m/s)						11.4					
Ω_0 (rpm)						12.1					

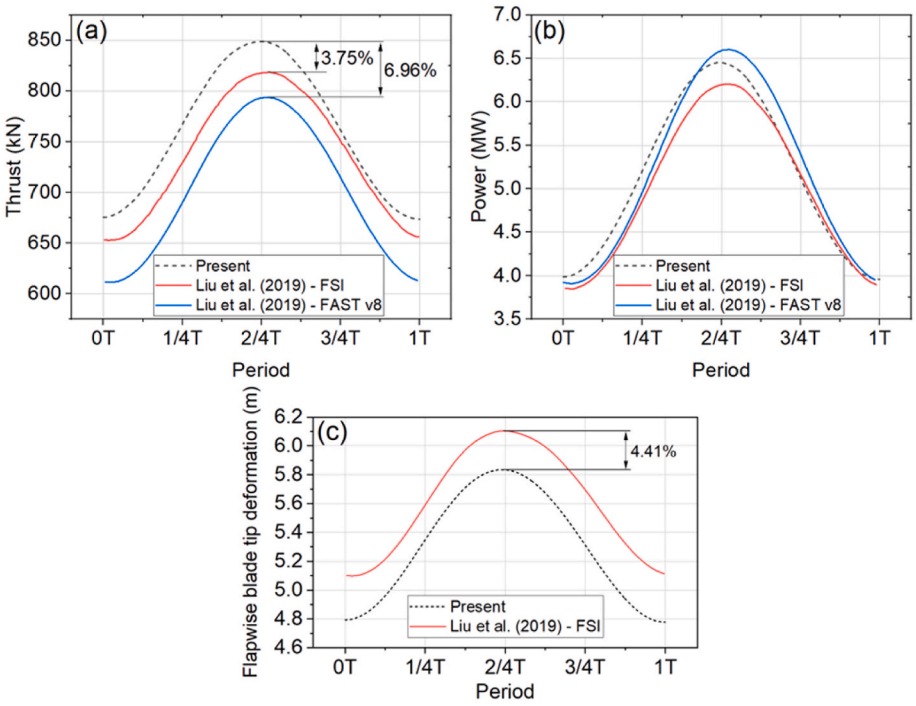

Fig. 8. Validation of (a) thrust, (b) power and (c) flapwise blade tip deflection within one surge period for LC3 (As = 2 m, T = 12 s).

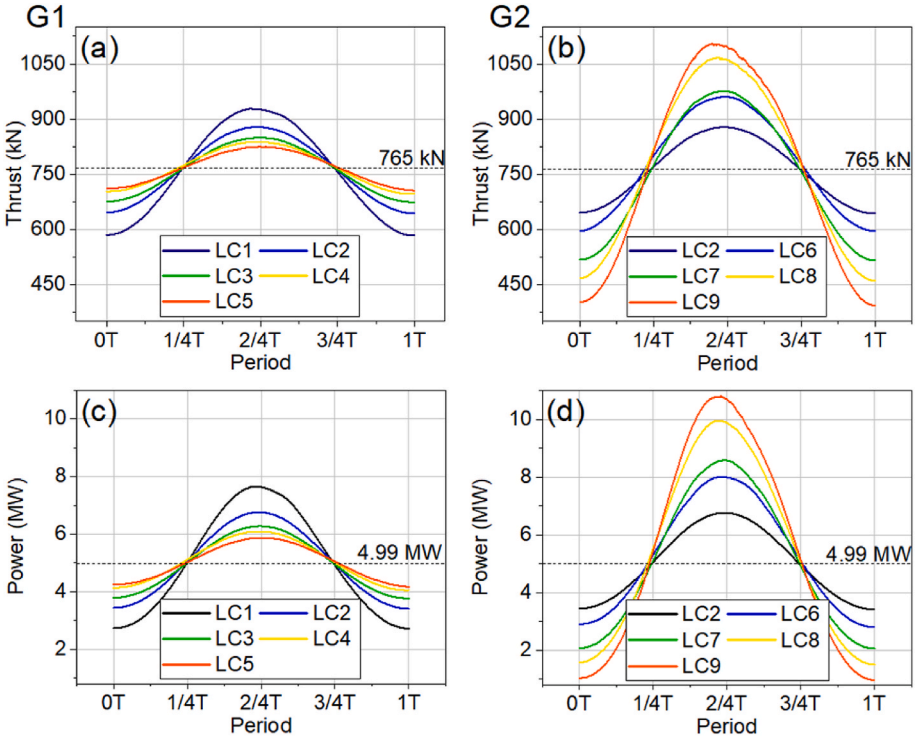

Fig. 9. Time history of the thrust and power within one normalised surge period.

blade, e.g. an increased fatigue stress and lower aerodynamic efficiency.

Fig. 11 display the maximum, minimum and averaged thrust and power among all load cases. To quantify the significance of the offsets between the extreme and averaged values, a modified standard deviation $\widetilde{\sigma}$ is used, formulated as:

$$\widetilde{\sigma} = \frac{\sigma}{Thrust_{avg}} \times 100\% \tag{14}$$

$$\sigma = \sqrt{\sum_{i=max,min} \frac{\left(Thrust_i - Thrust_{avg}\right)^2}{2}} \tag{15}$$

An example is from Fig. 11 (a), the $\widetilde{\sigma}$ decreases from 22.76 % to 7.73 %, showing that the aerodynamic thrust converges to the averaged thrust value as the surge period increases from LC1 to LC5. The power plots depicted in Fig. 11 (c) also shown a similar performance.

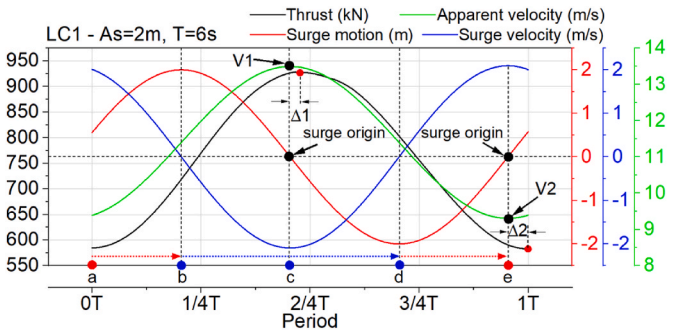

Fig. 10. Example of LC1 – demonstration for the delay of the aerodynamic thrust.

Comparatively, the thrust and power curves in G1 plots appears a more gradual and smoother evolution, while in G2 plots, the thrust and power curves under different surge amplitudes shown a less consistent evolution, where it is also reflected from the average curves from G1 and G2 plots (black dash line). This means that the FOWT aerodynamic performance can be more prone and sensitive to the varying surge amplitude rather than surge period.

Next, to give a more in-depth inspection to the aerodynamic performance of the blades, the instantaneous aerodynamic thrust distributions along a single blade are shown in Fig. 12. The thrust distributions for each load case are acquired from the corresponding moments when the max. flapwise deflections of the blade tip are reached.

In G1 plots, it can be seen that the curve of the thrust distribution shifts from high to low as the surge period increases. While in G2 plots, as the surge amplitude decreases, the thrust distributions curves shift downward, meaning that the thrusts become smaller. This also justifies the previously analyses as given for Fig. 9.

Furthermore, the zoom-in plots in G1 and G2 of the instantaneous aerodynamic thrust distributions reveals that the thrust occurring at the blade root and transitional region (r/R = [0.04, 0.16]) undergoes significant disturbance, indicating a pronounced nonlinear aerodynamic behaviour. Such aerodynamic nonlinearity becomes particularly evident in the load cases presented in G2, which might explain the less consistent evolution of the thrust and power curves as previously depicted in Fig. 11.

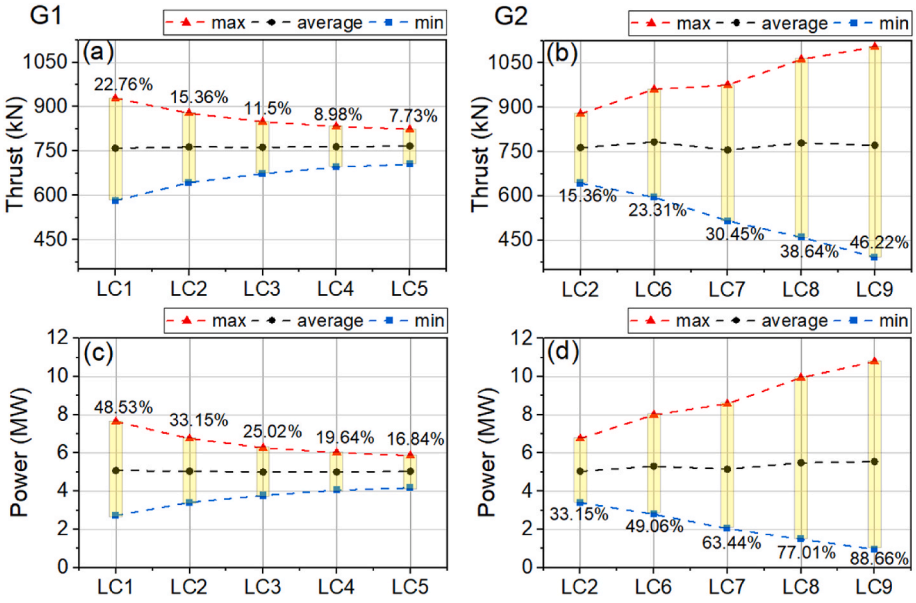

Fig. 11. Thrust and power variations for all load cases, grouped in G1 and G2.

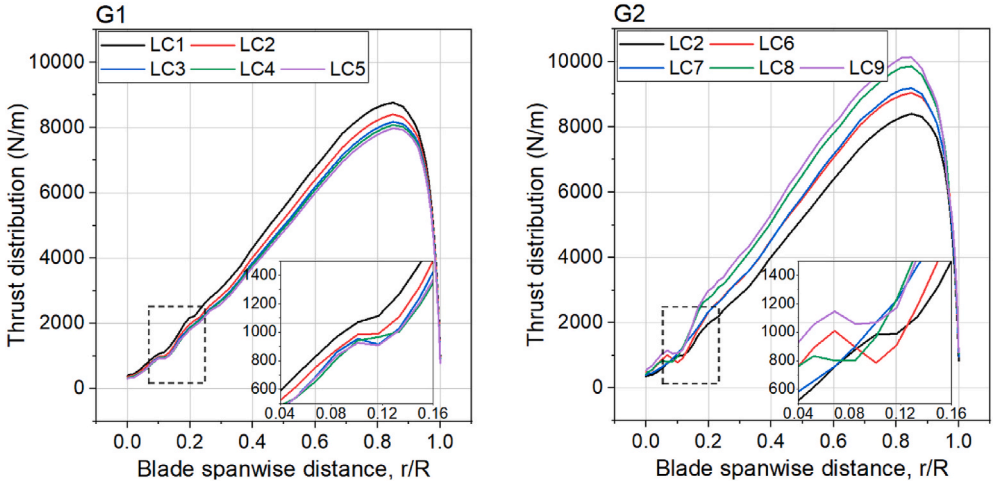

Fig. 12. Aerodynamic thrust distribution along the blade, comparisons between the load cases of (a). different surge periods and (b) different surge amplitudes.

To illustrate the fluid dynamics around the blade under different platform motion load cases, the fluid field contours of LC1, LC2 and LC9 are extracted. Note that the extracted fluid field results are in correspondence to the moment when the max. blade deflection occurs for each load case. Firstly, the comparisons of the pressure coefficients C_p on three cross-section locations on the blade (r/R = 0.3, 0.6 and 0.9) are shown in Fig. 13. The formulation of C_p is given as:

$$C_p = \frac{P_0 - P_\infty}{0.5\rho\left[U^2 + (\omega r)^2\right]} \tag{16}$$

where P_0 is the gauge pressure at the specified blade cross-section, P_∞ is defined as 0, representing the pressure at the infinite far field. The total flow speed relative to the blade includes both the freestream velocity and the rotational velocity, where r is the distance from the blade cross-section to the rotor centre, and ω is the angular velocity in rad/s.

In the C_p plots, LC9 shows the most significant variation compared to LC1 and LC2 across all cross-sections. At r/R = 0.3, the max. absolute values of C_p are 3.86 for LC9, 2.81 for LC2, and 2.55 for LC1. As r/R increases from 0.3 to 0.9 along the blade span, the variations in C_p become less noticeable. At r/R = 0.9, the C_p values on the pressure and suction sides for LC1 and LC2 almost overlap. For LC9, a positive pressure is found on the blade suction surface of the cross-section leading edge at r/R = 0.9, exerting a downward moment on the corresponding blade cross-section locations.

The contours below depicted the C_p distributions around the blade spanwise cross-section locations under LC1, LC2 and LC9, the max. limit of the legend has been set to $-C_p = 2$ for a clearer view of the nuance differences C_p distributions among three load cases.

The velocity field around the LC9 blade is shown in Fig. 14, illustrating the instantaneous velocity in the global X direction at different cross-sections along the blade span. The highest X velocity is seen at the leading edge of each blade section. Additionally, reverse flow occurs across all sections of the blade. From the root (r/R = 0.3) to the middle (r/R = 0.6), the reverse flow becomes more pronounced but then decreases in significance as it approaches the blade tip (r/R = 0.9).

This suggests the occurrence of the flow separation on the blade suction surface. The reasoning to this is that the blade is experiencing the largest aerodynamic thrust loads at this particular moment (when the max. blade deflection occurs), which is also when the relative flow velocity closes to the largest value within the platform surge period.

7.2. Blade deflections

In this section, the blade aeroelastic characteristics are indicated by the local deflection Δx, and global displacement X of the blade tip, as shown in Fig. 15. The relation between Δx and X is:

$$\Delta x = X - S(t) \tag{17}$$

where the definition of the surge displacement $S(t)$ was previously given in Eq. (12).

Notably, as depicted in LC9 deflection curve, the increase of surge amplitude results in prominent fluctuations in blade deflection, which brings additional higher-order frequencies to the blade dynamics. This can introduce extra aeroelastic instabilities to the blade structures. A Fast Fourier Transform (FFT) analysis will be given later on, to explain the aeroelastic instability as reflected in LC9 in detail.

To quantify the local deflections in G1 and G2 plots, the differences (in percentage) between the max. blade flapwise deflections Δx and the converged blade tip displacement of 5.4 m (in black dot line in Fig. 15), acquired from LC0, is given as listed in Table 6.

Additionally, based on the time history of blade deflections, the FFT analysis are conducted as depicted in Fig. 16 for load cases grouped in G1 and G2, respectively. From Fig. 16 (a), it is found the correspondence frequencies of each load case increases as the surge period decreases from LC5 (18 s) to LC1 (6 s). This suggests that a shorter surge period can introduce a more prominent nonlinear effect to the blade dynamics, which may result in greater dynamic instabilities to the blade structures.

In Fig. 16 (b), the excited second-order frequency of approximately 0.119 Hz is observed for all load cases from G2 results for the load cases with an identical surge period.

From the above analysis, it is found that the variations of the platform surge period can bring undesired second-order frequencies to the blade dynamics, resulting in blade structural instability that may impair the blade fatigue durability. However, it is found that the second-order frequency does not vary along with the change in surge amplitudes, thus, it is considered the blade fatigue performance will not be seriously affected by the surge amplitude variations.

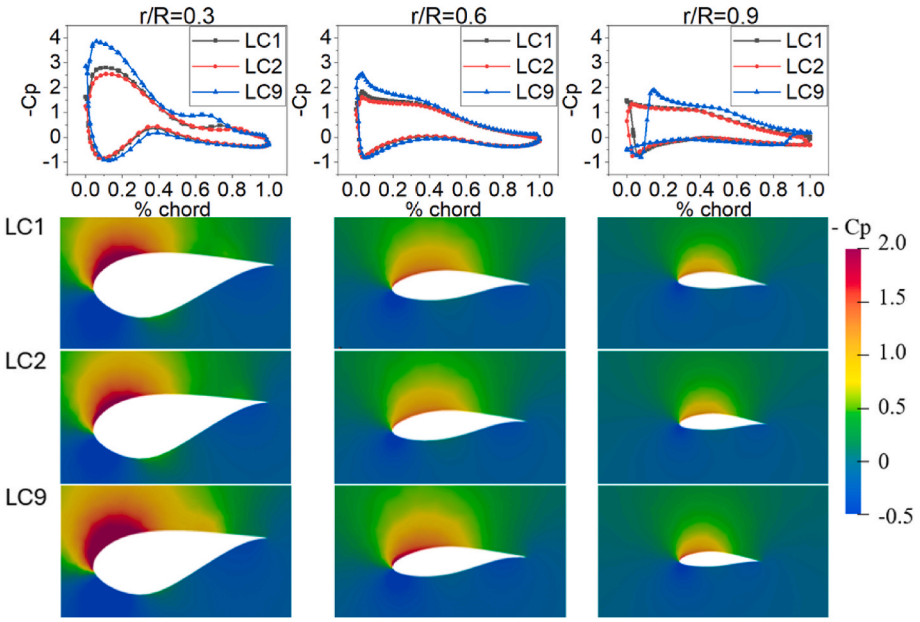

Fig. 13. Pressure coefficient (C_p) plots and contours at blade span r/R = 0.3, 0.6 and 0.9 for LC1, LC2 and LC9.

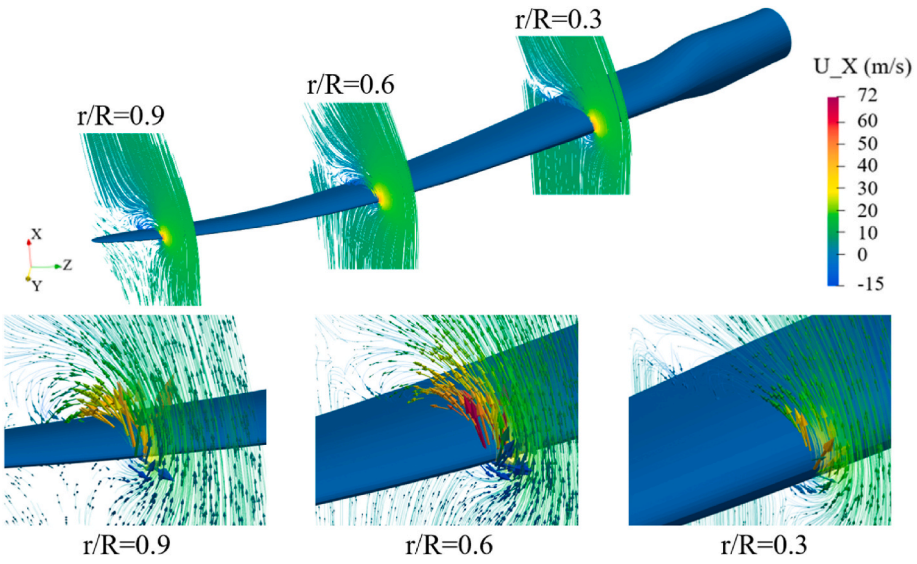

Fig. 14. Instantaneous X velocity contours at different blade spans, with streamline plotted for each blade span location.

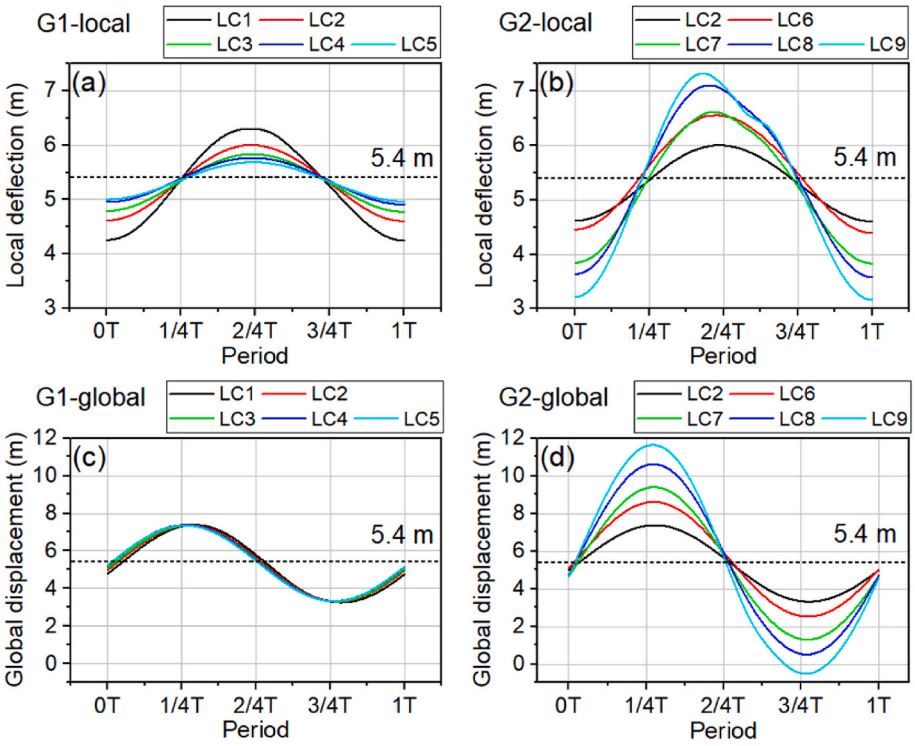

Fig. 15. Time history of the blade tip deflections and global displacements on flapwise direction for all load case.

Table 6
Max. local flapwise deflections of the blade tip for all load cases.

G1			G2		
Load cases	Δ*x* (m)	Diff	Load cases	Δ*x* (m)	Diff
LC0	5.400	/	LC0	5.400	/
LC1	6.304	16.75 %	LC2	6.003	11.16 %
LC2	6.003	11.16 %	LC6	6.554	21.38 %
LC3	5.835	8.06 %	LC7	6.618	22.55 %
LC4	5.769	6.84 %	LC8	7.105	31.58 %
LC5	5.687	5.32 %	LC9	7.327	35.69 %

The above results quantitatively evaluate the max. deflection of the blade under designated surge motions, this can be quite useful for determining the tower clearance of the blade during the designing process of the FOWT.

7.3. Stresses on the composite blade

The impacts of the platform motion to the blade structural stress performance are evaluated in this section. The stress analysis of the composite blade structure is conducted to reveal the stress conditions on multi-hierarchy of the blade structure, namely the blade shells, individual blade component (e.g. shear web), and the internal plies of the composite laminates.

Firstly, the Von Mises (VM) stresses on the composite blade suction surface are presented for LC1, LC3 and LC9, representing the shortest surge period, normal and largest surge amplitude conditions, respectively. As shown in Fig. 17(a) and (b) and (c), for each load case, the stresses on the blade from nine moments within one surge period were

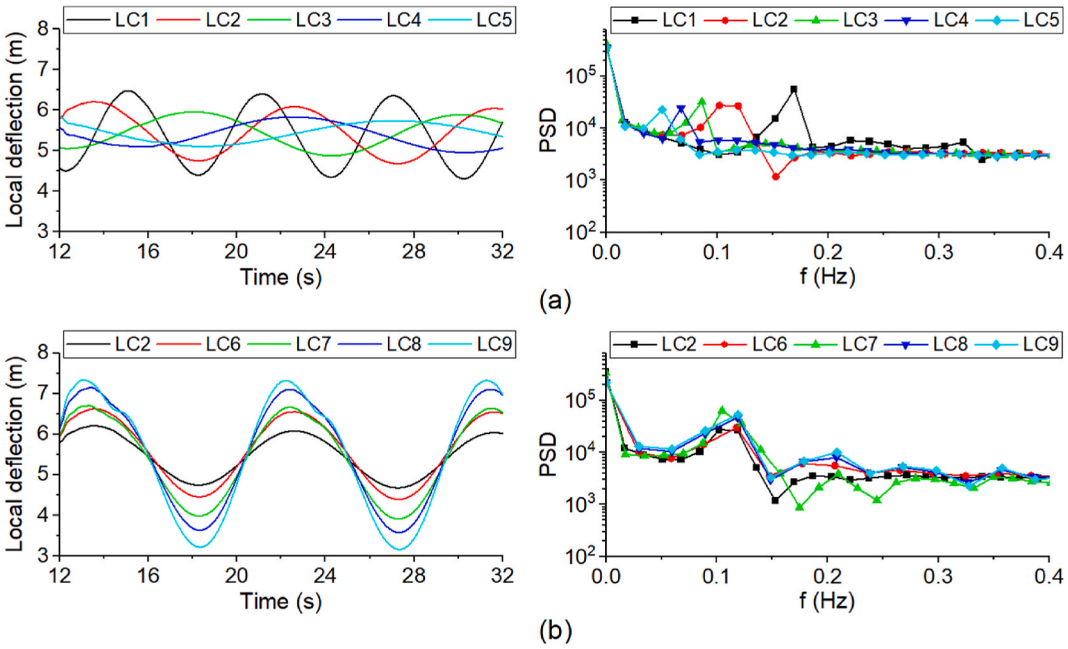

Fig. 16. FFT analysis for the blade flapwise deflections for (a). G1 and (b). G2 load cases.

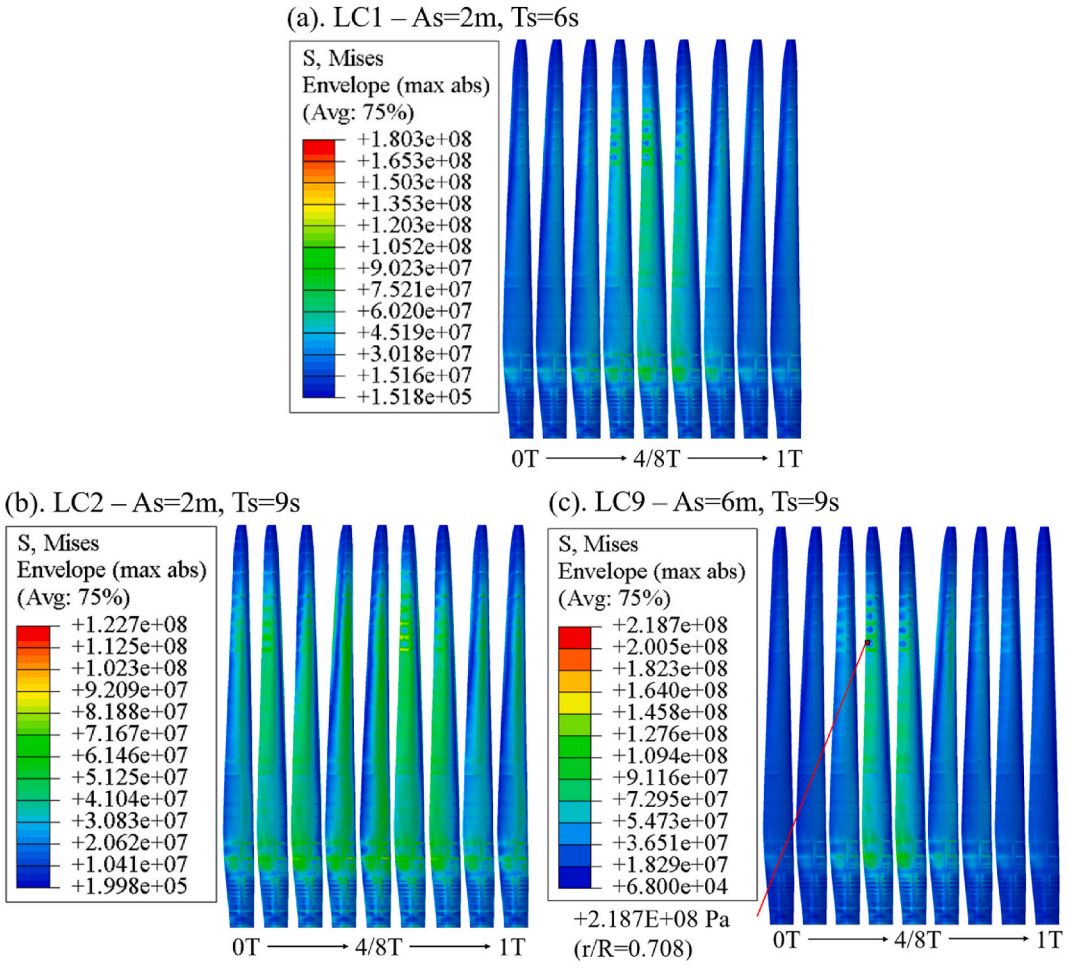

Fig. 17. VM stress distributions on the blade outer surface, for (a). LC1, (b). LC2 and (c). LC9. Unit in Pa.

obtained.

Fig. 17 (a) and (c) indicated the blade shell stress distribution for LC1 and LC9. It shows that at the 4/8T and the nearby region (i.e. when the large deflection occurs), the overall stress of the blade exhibits a greater amplitude compared to other moments. While for LC3 in Fig. 17 (b), due to the milder surge motion of LC3, the stress distributions on the blade shells exhibits smoother with less pronounced stress variations during the surge period, compared with LC1 and LC9.

Noting that in LC9, unlike the other two load cases, the global max. VM stress is observed at 3/8T, occurring at the trailing edge of the blade at a span of r/R = 0.708. To explain this, Fig. 18 shows the principal axial and shear stain components at 3/8T in the areas where blade span r/R = [0.68, 0.83]. A local buckling is observed as indicated by the stress distribution on the blade. From the strain distribution contours, a significant compression in local 1-direction at the trailing edge is observed, denoted by the negative strain (in blue) as shown in the SE1 contour. The '1-direction' and '2-direction' are defined as local directions relative to the shell element length (align with the direction of the blade span) and width (perpendicular to the direction of blade span), respectively (ABAQUS, 2009).

The blade deflection is amplified due to the platform motion induced loads, causing larger strains in the further span of the blade, where the stiffnesses are usually lower due to a smaller thickness of the blade shell structure comparing to that in the lower span area (e.g. the blade root).

Next, we inspect the stress distributions on the individual component shear webs since they are primarily designed for withstanding the shear forces and reinforcing the bending and torsional stiffness of the blade, meaning that the load conditions on the shear webs can be more severe, thus, a detailed check is necessary. The deployment of the shear webs on the NREL 5 MW reference wind turbine is demonstrated in Fig. 19.

An example of stress distributions on the shear web 1 for LC9 is presented in Fig. 20. As observed from the contours, the instantaneous local stress concentration shifts within one surge motion period, continuously jumping from the left to the right edge of the shear web during the surge motion. The max. VM stress concentration is observed at the 4/8T moment, with a magnitude of 155.1 MPa.

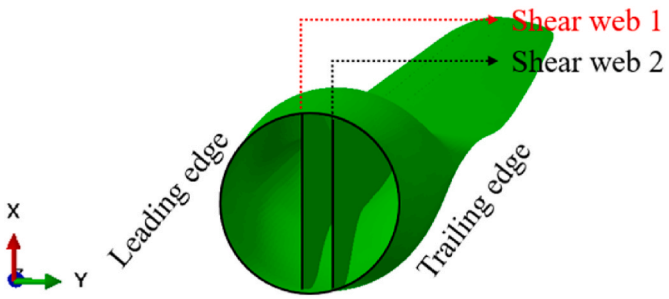

Fig. 19. Schematic diagram of the shear webs on the blade.

This clearly shows the time dependency of the stress concentration location and its magnitude. Such quantitative data can be helpful for determining the binding strength of the boundaries where the shear webs and spar caps are connected, based on which the engineers may optimize the strength of the connections between the two, and thus further improve the integrity and reliability of the blade.

Furthermore, the instantaneous internal in-ply stress distributions on the shear web 1 are resolved, corresponding to the moment when the blade reaches to the max. flapwise deflection for all load cases. A schematic diagram of the shear web sandwich structure is shown in Fig. 21. The shear web is composed of the unidirectional glass fibre Saertex laminates on the outer skins (in orange), with FOAM filling the cores (in blue).

Worth being noted that, in this study, a ply-to-ply modelling strategy is adopted for the shear web sandwich structure for the convenience of stress distribution demonstrations across each ply. Such modelling approach does not accurately reflect the manufacturing reality for the shear webs, where the interior FOAM stacks usually form a monolithic structure, rather than a ply-to-ply structure.

Therefore, a numerical validation using both modelling strategies has been conducted which confirms that the predicted max. VM stress shows almost identical distribution across the shear web sandwich structures, as shown in Fig. 22. In the monolithic model, a sufficient

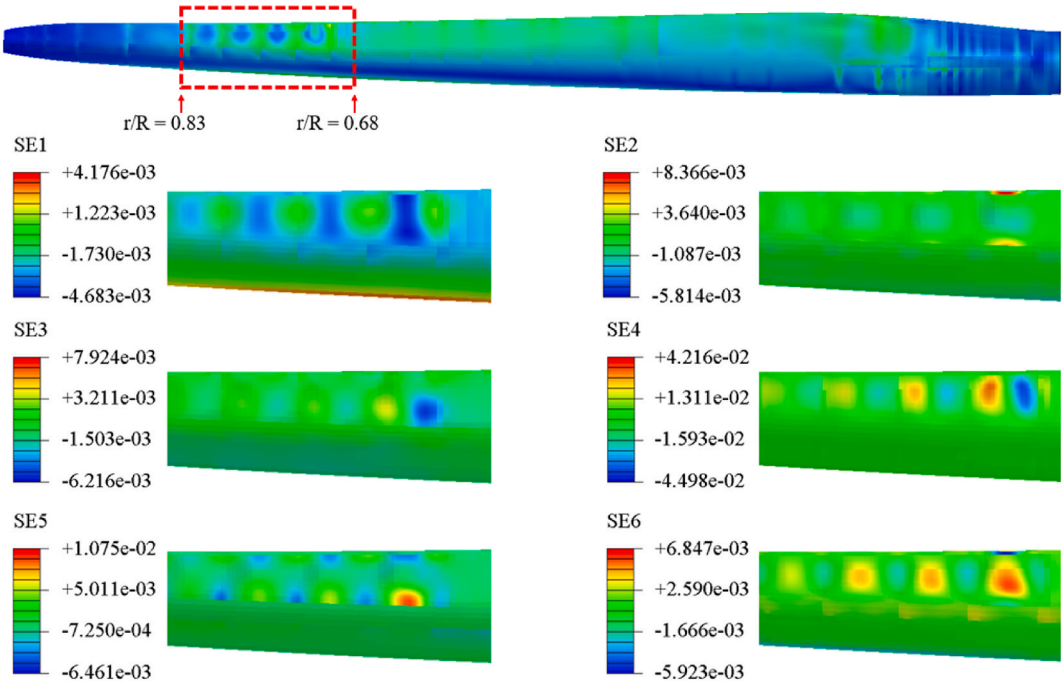

Fig. 18. Section strain contours on the blade span r/R = [0.68, 0.83] under LC9 at 3/8T. Six components are: SE1 – direct membrane strain in 1-direction; SE2 – direct membrane strain in 2-direction; SE3 – shear membrane strain in 1–2 plane; SE4 – transverse shear strain in 1-direction; SE5 – transverse shear strain in 2-direction; SE6 – strain in element thickness direction (ABAQUS, 2009).

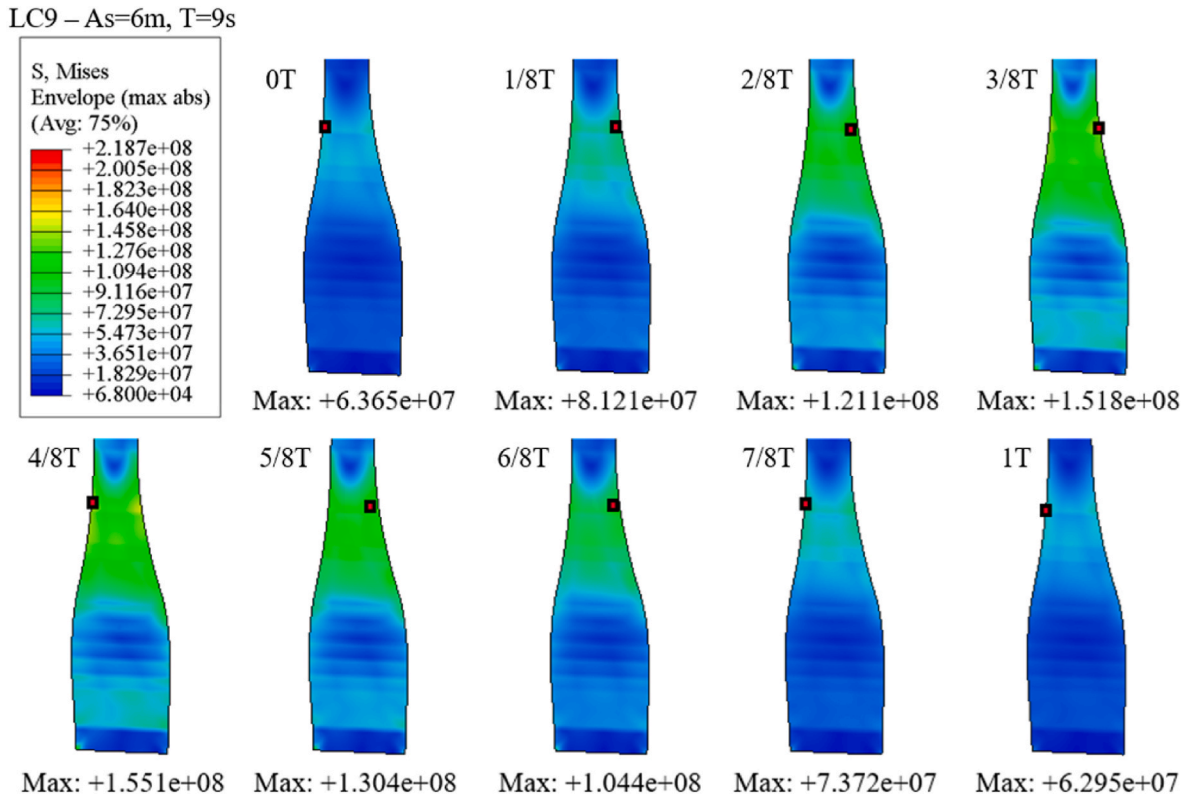

Fig. 20. VM stress distributions on the shear web 1 for nine moments in a complete surge period of LC9, unit in Pa.

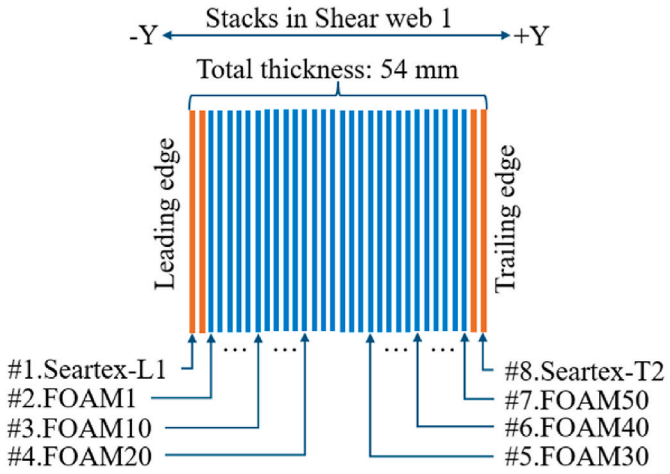

Fig. 21. Schematic diagram of the shear web sandwich structure.

number of integration points on the thickness direction are given to provide enough resolution for detailed stress inspections. Table 7 lists the selected plies used to demonstrate stress distributions across shear web 1.

Fig. 23 shows a non-consecutive in-ply stress distribution, especially for the adjacent plies of Saertex-L1 and FOAM1, a noticeable decrease of the stress magnitude with a shift of location is observed. The max. VM stress magnitudes on the Saertex and FOAM plies are 132.5 MPa and 1.826 MPa, respectively, showing a difference of two orders of magnitude. This is due to the significant stiffness drop from the composite laminate skin (glass fibre reinforced polymer) to the FOAM core, where the strain distribution is identical to all plies on the shear webs.

Additionally, the shifts in location of the max. VM stress across the FOAM plies are observed, from the root of the shear web (on -X direction) to the transitional area of the shear web (on + X direction). The VM stress distributions for FOAM plies in the shear web 1 under all load cases are firstly displayed in Fig. 24. The max. VM stress depicted here is an equivalent metric while it cannot explain such shifts phenomena comprehensively.

Thereby, the direct (S11 and S22) and shear (S12) stress components are quantified and depicted in Fig. 25. The variations in each stress components max. magnitude across the FOAM plies exhibit a clear bi-linear characteristic (as the max. VM stress in Fig. 23). The locations for each max. stress component in blade spanwise direction are indicated in red, denoting the abrupt changes (i.e. the shifts) of the local max. stress occurrence locations across the FOAM plies.

It is seen that the shifts in blade spanwise of the local max. stress usually occur at the pivot points of the bi-linear stress curves for each stress components. This suggests that the evolution of each stress component is discontinuous, accompanied with sudden changes in the occurrence locations of the max. stresses.

From the results, the magnitudes of all stress components exhibit a bi-linear pattern across the shear web thickness direction, which is a logical representation of the effects of torsional loading acting on the shear web sandwich structure. Besides, this is also consistent with the design purpose of the blade shear web as it withstands torsional loads, which typically can cause a linear variation in stress in structure (here, the FOAM plies).

7.4. Relations between blade stresses and surge motions

From the previous analysis, it is recognised that the max. local VM stress concentration often occurs on the shear webs. In this section, we presented the correlations between the blade Max. VM stress and the surge periods and amplitudes. Here, the resolved VM stress is a global max. stress, reflecting the largest stress that the blade could potentially experience under each load case.

To provide quantitative evaluation of the amplification of the stress

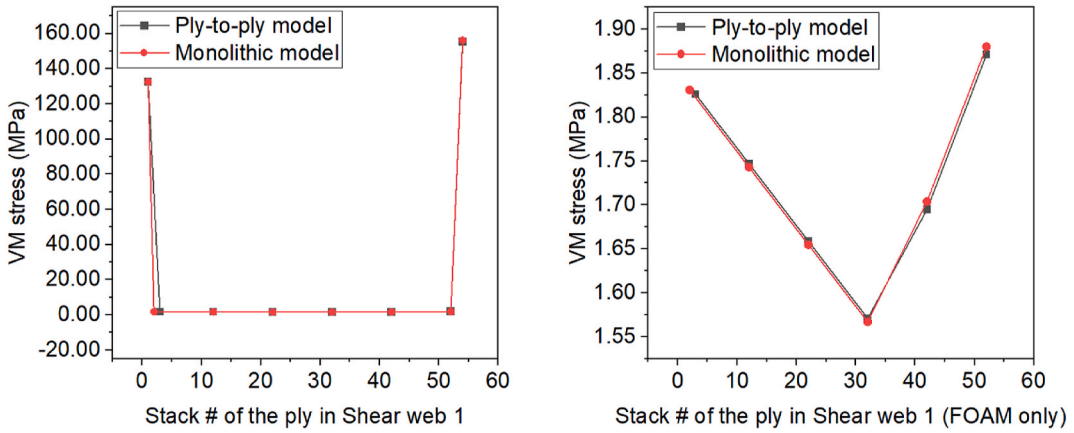

Fig. 22. Numerical validation for stress predictions across shear web 1 plies using ply-to-ply and monolithic models, at max. flapwise blade deflection under the LC9.

Table 7
Selections of plies (in shear web 1) for VM stress distribution demonstration.

Name of ply	Thickness of each ply	Stack # of the ply
#1.Saertex-L1	1 mm	1
#2.FOAM1	1 mm	3
#3.FOAM10	1 mm	12
#4.FOAM20	1 mm	22
#5.FOAM30	1 mm	32
#6.FOAM40	1 mm	42
#7.FOAM50	1 mm	52
#8.Saertex-T2	1 mm	54

under surge load cases, the blade max. VM stress resolved under the bottom-fixed condition (no platform motion) is retrieved from our previous study (Deng et al., 2024), denoted as σ_{max_0} for comparison, where σ_{max_0} is 103.5 MPa corresponding to the moment at the infinite.

From Fig. 26 (a) below, a significant increase by +74.11 % of the max. VM stress is observed for the surge period T = 6 s, compared to the σ_{max_0}. While during the surge period T ∈ [9, 12] s, the max. VM stress variations against the σ_{max_0} are less than 20 %. It is clear that the max. VM stress on the shear web is much more prone to a small period (higher frequency) of surge motion. Even though the situation of T = 6 s is not a common load case scenario, this finding still quantifies the potential stress consequences under an 'extreme' load case, showing the capability of the adopted FSI analysis framework.

Similarly, the σ_{max_0} acquired from the previous study is used to give a clear comparison of the variation of the max. VM stress that the blade experiences under the load cases among different surge amplitudes. As can be seen from Fig. 26 (b), a linear evolution of the max. VM stress across different surge amplitude load cases is observed.

A linear fit is implemented as depicted in red dash line, the correlation coefficient (R^2) of the linear fit is 0.9822, indicating a strong linear relationship between surge amplitude and the max. VM stress. This linear relationship allows researchers to easily quantify the impact of variations in surge amplitude on the blade's max. VM stress. For instance, within the given range of surge amplitudes, an increase in surge amplitude by 1 m can result in an approximate increase of 53 MPa in the max. VM stress.

Although in LC9, a 6-m surge amplitude is an uncommon case for FOWT operating conditions, this linear relationship can be effectively

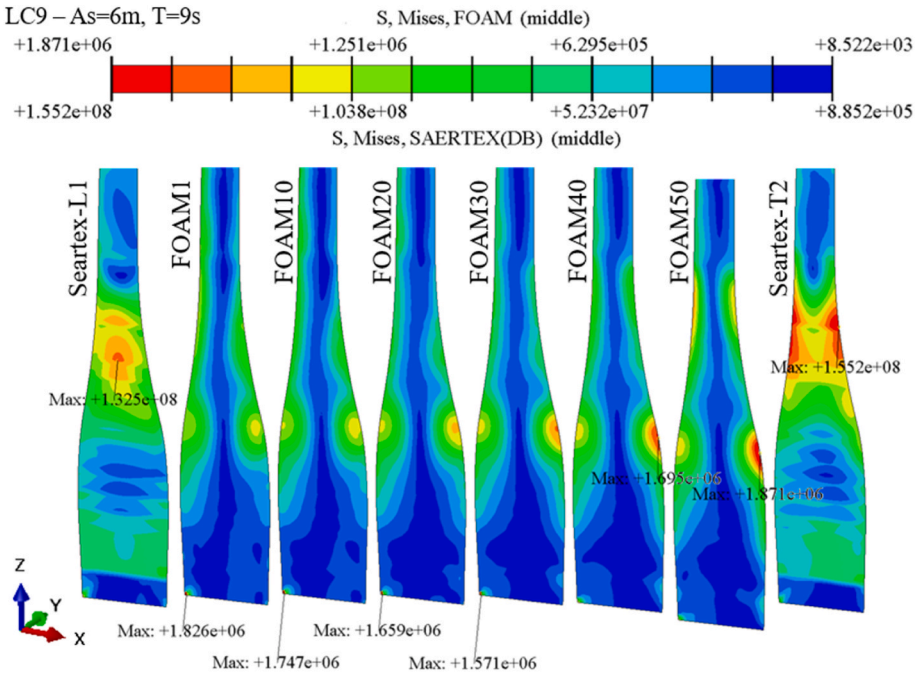

Fig. 23. VM stress distributions of selected plies on shear web 1, at max. flapwise blade deflection under the LC9, unit in Pa.

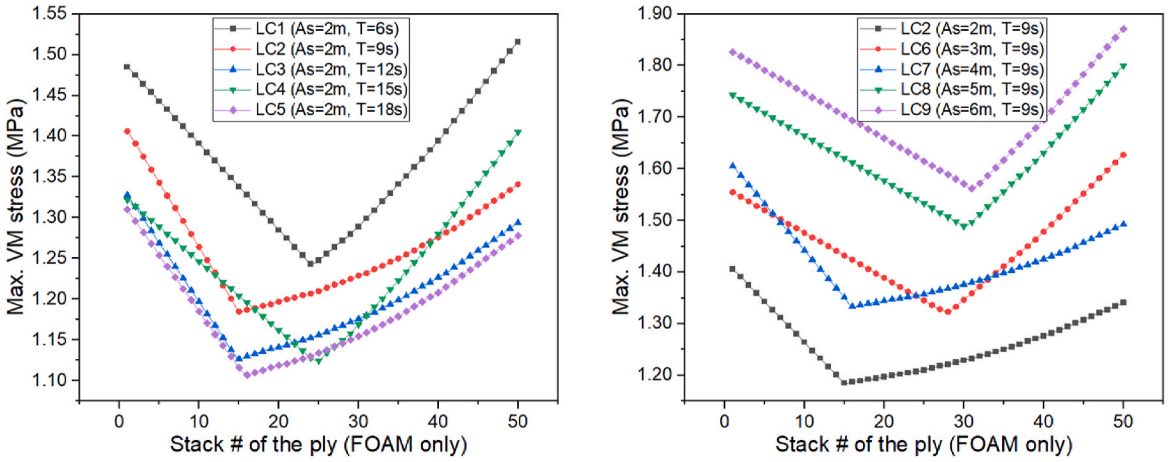

Fig. 24. Max. VM stress across the FOAM plies for all load cases, at max. flapwise blade deflection under the LC9.

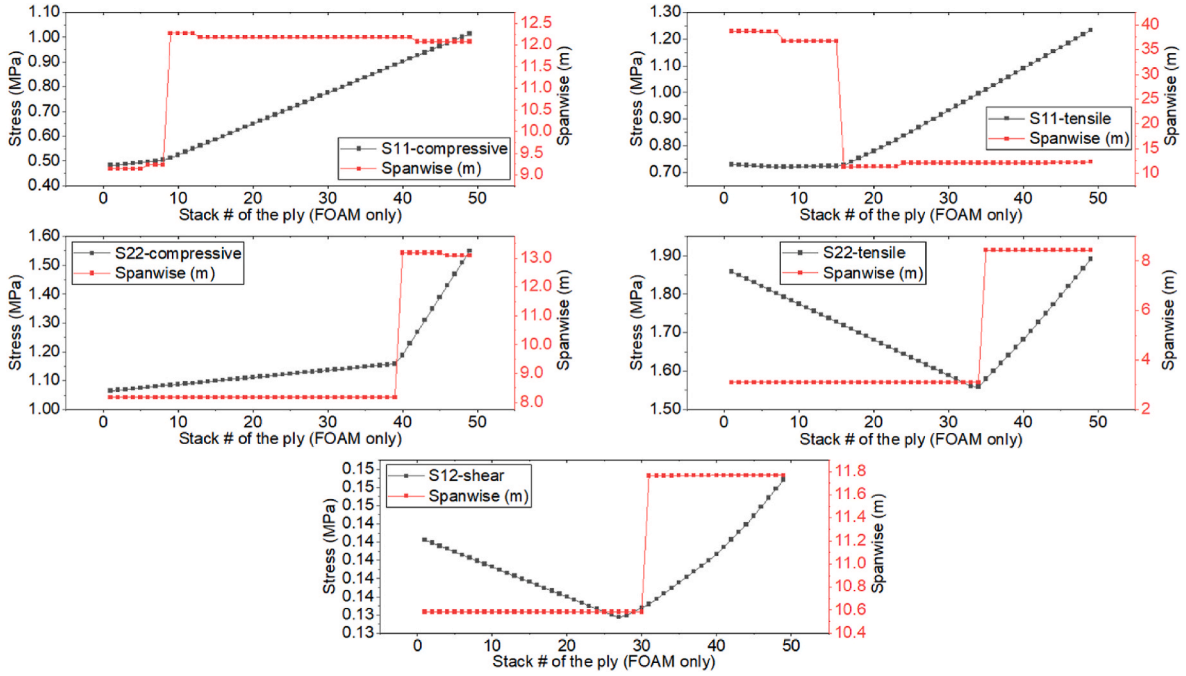

Fig. 25. Max. direct and shear stress components of FOAM plies on shear web 1, with correspondence occurrence location on blade spanwise direction. At max. flapwise blade deflection under the LC9.

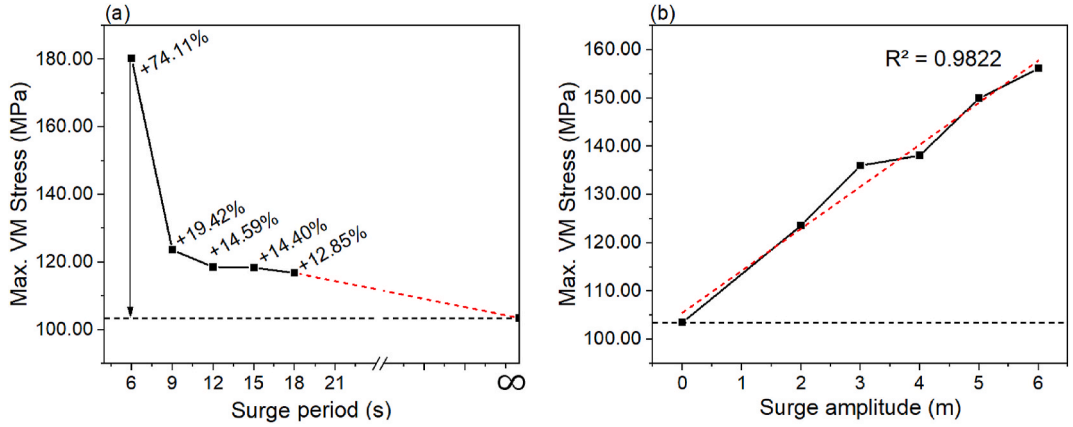

Fig. 26. Relationships of the (a). max. VM stress vs. surge periods, (b). max. VM stress vs. surge amplitudes.

captured by our presented FSI framework. This assists designers in quickly determining whether the blade strength can withstand the certain surge amplitudes for new FOWT designs, thereby ensuring the safety and reliability of the blade under various surge conditions.

8. Conclusions and remarks

This study comprehensively investigated the aeroelastic performances of composite wind turbine blades under various prescribed surge motions, replicating the regular platform surge motions of a NREL 5 MW FOWT. The main findings are presented in terms of blade aerodynamic, aeroelastic behaviours and structural stress performances.

The aerodynamic thrust and power from nine load cases are examined, where the variations are quantified by the modified standard deviation $\widetilde{\sigma}$. As the surge period increases from 6 s to 18 s for LC1 – LC5, the percentage of the thrust deviation decreases from 22.76 % to 7.73 %. While for LC2 – LC9, where the surge amplitude increases from 2 m to 6 m, the $\widetilde{\sigma}$ of the thrust increases from 15.36 % to 46.22 %. The distributions of aerodynamic thrust also support this finding by depicting the thrust force distributions along the blade for each load case. Additionally, a flow disturbance is observed near the blade root and transitional area where r/R = [0.04, 0.16].

An aerodynamic thrust delay with respect to the relative velocity on the FOWT is observed. Due to the interactions between the flexible blade and surrounded wind flow field, the occurrence of the max. thrust and the largest relative velocity are not exactly synchronised with each other. Especially for the severer load cases, such asymmetry performance becomes more prominent. This explains partially for the aeroelastic instabilities of an FOWT.

In the FFT analysis for the flapwise deflections in G1 results, the second-order frequencies with non-negligible amplitudes are observed. This suggests that a shorter surge period can introduce additional higher-order frequency excitation to the blade, which is undesired for the blade fatigue durability. This is an extensive topic that can be further investigated in the future.

Due to the intensive interactions between the fluid and structure fields, the blade aerodynamics and elasticity is strongly influenced by the prescribed surge motion load cases. Generally, the correlation between surge period and amplitude with the blade max. VM stress is opposite.

A linear corelation is found between the max. VM stress and surge amplitude. This can be useful for blade designing purposes as it provides a function with good fit for preliminary determining the largest VM stress that a blade may experience under a given surge amplitude. Even though such corelation can be case specific, it still reveals the qualitative relations between the presented variables.

Identifications of stress on blade component level revealed that the shear webs near the blade root and transitional areas are critical locations that are prone to local stress concentrations. This especially necessitates local inspections for the blade structural integrity under severe load cases. Besides, the in-ply VM stress distributions on the shear web 1 comprehensively demonstrated the non-consecutive stress evolution characteristics, with observations, e.g. the significant drop in stress magnitudes between the plies with different material properties, and the noticeable location shifts of max. stress across the FOAM core in-ply structure.

This study directly defines the platform motions by an evenly-spaced, pre-defined sinusoidal function, which is a reasonable reflection of regular wave conditions. Despite the noted limitations that such definition may deviate from the actual scenario of sophisticated ocean conditions, many peer studies have adopted sinusoidal motion prescriptions in cases where blade aerodynamics dominated by surge platform motions are of interest.

Focusing on the composite blade, we investigated the aeroelastic impacts to the composite structural stress performances, revealing the relationships between platform motion conditions and blade's aeroelastic performance. The concluded insights can still contribute to a further understanding of the aeroelastic behaviours of composite wind turbine blades. In future works, by conducting the fully-coupled aero-hydro-elastic numerical studies, more realistic platform motion data can be acquired and implemented, thus offers a more realistic reflection of the actual FOWT.

Nonetheless, this work provides a foundation of effective analysing tools for such future studies. It can also be used for further optimizations and validations for more durable and reliable FOWT systems when the considerations of composite properties are required.

CRediT authorship contribution statement

ZhongSheng Deng: Writing – original draft, Visualization, Validation, Methodology, Investigation, Formal analysis, Data curation, Conceptualization. **Qing Xiao:** Writing – review & editing, Supervision, Resources, Project administration, Investigation, Conceptualization. **Liu Yang:** Writing – review & editing, Supervision, Conceptualization. **YuanChuan Liu:** Software, Resources, Methodology. **Enhao Wang:** Writing – review & editing.

Declaration of competing interest

The authors declare that they have no known competing financial interests or personal relationships that could have appeared to influence the work reported in this paper.

Acknowledgements

The first author thanks for the High Performance Computing support from the Cirrus UK National Tier-2 HPC Service at EPCC (http://www.cirrus.ac.uk) funded by the University of Edinburgh and EPSRC (EP/P020267/1) and ARCHIE-WeSt High-Performance Computer (www.archie-west.ac.uk) based at the University of Strathclyde.

References

ABAQUS, 2009. ABAQUS Analysis User's Manual, v6.6.
Bauchau, O.A., Nemani, N., 2021. Modeling viscoelastic behavior in flexible multibody systems. Multibody Syst. Dyn. 51 (2), 159–194.
Bir, G.S., 2001. Computerized method for preliminary structural design of composite wind turbine blades. J. Sol. Energy Eng. 123 (4), 372–381.
Cesnik, C.E.S., Hodges, D.H., 1997. VABS: a new concept for composite rotor blade cross-sectional modeling. J. Am. Helicopter Soc. 42 (1), 27–38.
Chandar, D., Gopalan, H., 2016. Comparative Analysis of the Arbitrary Mesh Interface (AMI) and Overset Methods for Dynamic Body Motions in OpenFOAM. In 46th AIAA Fluid Dynam. Conf.
Chen, H., Yu, W., Capellaro, M., 2010. A critical assessment of computer tools for calculating composite wind turbine blade properties. Wind Energy 13 (6), 497–516.
Cheng, P., Huang, Y., Wan, D., 2019. A numerical model for fully coupled aero-hydrodynamic analysis of floating offshore wind turbine. Ocean Eng. 173, 183–196.
Dai, L., Zhou, Q., Zhang, Y., Yao, S., Kang, S., Wang, X., 2017. Analysis of wind turbine blades aeroelastic performance under yaw conditions. J. Wind Eng. Ind. Aerod. 171, 273–287.
De Vaal, J.B., Hansen, M.L., Moan, T., 2014. Effect of wind turbine surge motion on rotor thrust and induced velocity. Wind Energy 17 (1), 105–121.
Deng, Z., Xiao, Q., Huang, Y., Yang, L., Liu, Y., 2024. A general FSI framework for an effective stress analysis on composite wind turbine blades. Ocean Eng. 291, 116412.
Dose, B., Rahimi, H., Herráez, I., Stoevesandt, B., Peinke, J., 2018. Fluid-structure coupled computations of the NREL 5 MW wind turbine by means of CFD. Renew. Energy 129, 591–605.
Edwards, E.C., Holcombe, A., Brown, S., Ransley, E., Hann, M., Greaves, D., 2023. Evolution of floating offshore wind platforms: a review of at-sea devices. Renew. Sustain. Energy Rev. 183, 113416.
Fang, Y., Li, G., Duan, L., Han, Z., Zhao, Y., 2021. Effect of surge motion on rotor aerodynamics and wake characteristics of a floating horizontal-axis wind turbine. Energy 218, 119519.
Fritz, E.K., Ferreira, C., Boorsma, K., 2022. An efficient blade sweep correction model for blade element momentum theory. Wind Energy 25 (12), 1977–1994.
Ghiringhelli, G.L., Masarati, P., Mantegazza, P., 2000. Multibody implementation of finite volume C beams. AIAA J. 38 (1), 131–138.
Hollaway, L.C., 2013. 19 - sustainable energy production: key material requirements. In: Bai, J. (Ed.), Advanced Fibre-Reinforced Polymer (FRP) Composites for Structural Applications. Woodhead Publishing, pp. 705–736.

Jasak, H., Jemcov, A., Tukovic, Z., 2007. OpenFOAM: A C++ library for complex physics simulations.
Jasak, H., Tukovic, Z., 2006. Automatic mesh motion for the unstructured finite volume method. Trans. FAMENA 30, 1–20.
Lamei, A., Hayatdavoodi, M., 2020. On motion analysis and elastic response of floating offshore wind turbines. J. Ocean Eng. Marine Energy 6 (1), 71–90.
Lienard, C., Boisard, R., Daudin, C., 2020. Aerodynamic behavior of a floating offshore wind turbine. AIAA J. 58 (9), 3835–3847.
Liu, Y., Xiao, Q., Incecik, A., Peyrard, C., 2019. Aeroelastic analysis of a floating offshore wind turbine in platform-induced surge motion using a fully coupled CFD-MBD method. Wind Energy 22 (1), 1–20.
Masarati, P., Morandini, M., Mantegazza, P., 2014. An efficient formulation for general-purpose multibody/multiphysics analysis. J. Comput. Nonlinear Dynam. 9, 041001.
Menter, F.R., Kuntz, M., Langtry, R., 2003. Ten years of industrial experience with the SST turbulence model. Turbulence, heat and mass transfer 4 (1), 625–632.
Miao, W., Li, C., Wang, Y., Xiang, B., Liu, Q., Deng, Y., 2019. Study of adaptive blades in extreme environment using fluid–structure interaction method. J. Fluid Struct. 91, 102734.
Micallef, D., Sant, T., 2015. Loading effects on floating offshore horizontal axis wind turbines in surge motion. Renew. Energy 83, 737–748.
Otter, A., Murphy, J., Pakrashi, V., Robertson, A., Desmond, C., 2022. A review of modelling techniques for floating offshore wind turbines. Wind Energy 25 (5), 831–857.
Resor, B.R., 2013. Definition of a 5MW/61.5m wind turbine blade reference model. https://www.osti.gov/servlets/purl/1095962.
Sayed, M., Lutz, T., Krämer, E., Shayegan, S., Wüchner, R., 2019. Aeroelastic analysis of 10 MW wind turbine using CFD–CSD explicit FSI-Coupling approach. J. Fluid Struct. 87, 354–377.
Simeon, B., 2006. On lagrange multipliers in flexible multibody dynamics. Comput. Methods Appl. Mech. Eng. 195 (50), 6993–7005.
SIMULIA, 2014. ABAQUS Theory Manual.
Sun, Q., Li, G., Duan, L., He, Z., 2023. The coupling of tower-shadow effect and surge motion intensifies aerodynamic load variability in downwind floating offshore wind turbines. Energy 282, 128788.
Tran, T.T., Kim, D.-H., 2016. A CFD study into the influence of unsteady aerodynamic interference on wind turbine surge motion. Renew. Energy 90, 204–228.
Wang, L., Liu, X., Kolios, A., 2016a. State of the art in the aeroelasticity of wind turbine blades: aeroelastic modelling. Renew. Sustain. Energy Rev. 64, 195–210.
Wang, L., Quant, R., Kolios, A., 2016b. Fluid structure interaction modelling of horizontal-axis wind turbine blades based on CFD and FEA. J. Wind Eng. Ind. Aerod. 158, 11–25.
Wen, B., Tian, X., Dong, X., Peng, Z., Zhang, W., 2017. Influences of surge motion on the power and thrust characteristics of an offshore floating wind turbine. Energy 141, 2054–2068.
Yang, L., Liao, K., Ma, Q., Ma, G., Sun, H., 2023. Investigation of wake characteristics of floating offshore wind turbine with control strategy using actuator curve embedding method. Renew. Energy 218, 119255.
Yu, D.O., Kwon, O.J., 2014. Predicting wind turbine blade loads and aeroelastic response using a coupled CFD–CSD method. Renew. Energy 70, 184–196.
Yu, W., Volovoi, V.V., Hodges, D.H., Hong, X., 2002. Validation of the variational asymptotic beam sectional analysis. AIAA J. 40 (10), 2105–2112.
Zhang, W., Calderon-Sanchez, J., Duque, D., Souto-Iglesias, A., 2024. Computational fluid dynamics (CFD) applications in floating offshore wind turbine (FOWT) dynamics: a review. Appl. Ocean Res. 150, 104075.
Zhang, Y., Song, Y., Shen, C., Chen, N.-Z., 2023. Aerodynamic and structural analysis for blades of a 15MW floating offshore wind turbine. Ocean Eng. 287, 115785.
Zhang, Z., Zhang, C., Qiao, Y., Zhou, Y., Wang, S., 2023. Design and mass optimization of numerical models for composite wind turbine blades. J. Mar. Sci. Eng. 11 (1), 75.